Implementation of a non-Hertzian Contact Model for Railway Dynamics

Hugo Magalhães[1], Filipe Marques[2], Binbin Liu[3], João Pombo[1,4], Paulo Flores[2], Jorge Ambrósio[1], Stefano Bruni[3]

[1] LAETA, IDMEC, Instituto Superior Técnico, Universidade de Lisboa, Avenida Rovisco Pais 1,
1049-001 Lisboa, Portugal, {hugomagalhaes,jorge.ambrosio}@tecnico.ulisboa.pt
[2] MIT-Portugal Program, CMEMS-UMinho, Departamento de Engenharia Mecânica, Universidade do Minho,
Campus de Azurém, 4804-533 Guimarães, Portugal, {fmarques,pflores}@dem.uminho.pt
[3] Dipartimento di Meccanica, Politecnico di Milano, Via La Masa 1,
Milano 20156, Italy, {binbin.liu,stefano.bruni}@polimi.it
[4] Institute of Railway Research, School of Computing and Engineering, University of Huddersfield, UK and ISEL, IPL,
Lisboa, Portugal, j.pombo@hud.ac.uk

Abstract — The development of wheel-rail contact models is an active topic of research, in which more accurate and reliable methodologies are required to improve the realism of multibody simulations while reducing the computational effort. However, their implementation in a multibody software consists of a challenging task for itself. This paper presents a generalized strategy for the implementation of non-Hertzian contact models. This new methodology is split into the following steps: determination of points of contact; identification of the undeformed distance function; determination of the contact patch; and calculation of the normal and tangential forces which are computed according to the contact conditions and the theories used. Here, the normal force is determined with the Kik-Piotrowski model, while the tangential forces are obtained from the interpolation of the Kalker Book of Tables for Non-Hertzian contact patches. To demonstrate the proper implementation of the new methodology, static and dynamic simulations have been performed. First, a static wheel-rail interaction at different slip conditions is simulated being observed a good agreement with respect to the results obtained from CONTACT. Secondly, a dynamic simulation of a bogie running in a tangent track is considered, in which the contact developed respect the Hertzian conditions. Thus, a comparison between the Hertzian approach and the proposed methodology is possible, being discussed the slight differences between the results obtained from both simulations. Besides the proposed implementation is 4.5 times slower than the Hertzian method considered in this work, for the case study presented in this work, the proposed methodology allows to deal with non-Hertzian contact.

1 Introduction

In railway dynamics, the vehicle-track interaction plays a key role not only on the track loading, but also on the vehicle dynamics, namely, in terms of running safety and ride characteristics [1]. This engineering field has been more and more studied through multibody simulations in which railway vehicles running in tracks at real operation conditions are analysed in a virtual environment [2]. A crucial ingredient of such simulations is the wheel-rail contact model which represents the forces developed over the wheel-rail contacting area [3]. Besides several dedicated wheel-rail contact models have been proposed, formulation for their implementation in

multibody software still lacks. In this paper, it is proposed a methodology to implement a non-Hertzian contact models in multibody software.

To perform a multibody simulation of a railway vehicle running a track, the vehicle, track and vehicle-track interaction models are required. The multibody model of the vehicle consists of a set of bodies that are interconnected by kinematic joints and/or force elements that represent the suspension system of the vehicle [4], [5]. The track model consists of two surfaces, representing the left and right rails, which constrain the motion of the wheels due to forces developed in the wheel-rail contacting areas. The track modelling consists of a geometric parameterization problem, namely, the rails position and orientation are defined [6], [7], and, if the track flexibility is important, the mechanical properties of the infrastructure must be considered [8]. In turn, the wheel-rail contact model represents the forces developed in the interference between the wheel and rail contact [3]. Thus, the solution of the forward dynamics problem, defined by a set of differential algebraic equations, is obtained by using a proper integrator algorithm [9]. The result of the simulation includes the time history of vehicle motion and forces developed in the multibody system, such as, the wheel-rail contact forces.

The wheel-rail contact consists of two bodies that contact in a region where local deformations occurs and normal and tangent forces are transmitted over the contacting area [10]. To represent such phenomena, many models available in the literature can be used [3]. The selection of the model consists of a trade-off between accuracy and computational effort and depends on the objective of the study. Rigid contact models can be employed, in which the contact between the wheel and rail consists of a point defined by a geometric constraint represented by reaction forces [11]. This method is fast but there is no information of the contact patch and hence the pressure distribution cannot be determined. For the elastic contact, virtual penetration is often considered, being possible the calculation of forces distributed in a determined contact patch. Under the Hertzian contact conditions, the contact patch exhibits an elliptic shape that can be determined based on the surface curvatures at the main contact point and the mechanical properties of the contacting surfaces [10]. This approach has been used in the wheel-rail contact methodology proposed by Pombo *et al* [12]. In turn, for non-Hertzian conditions, the neighbourhood of the main contact point must be taken into account to determine the undeformed distance function, that is, the distance between the wheel and rail surfaces. Different approaches can be used to deduce the non-elliptic contact patch, as it is presented in [13]. Thus, the normal force transmitted in the contact patch can be determined. For Hertzian contact, the model with hysteresis damping proposed by Lankarani and Nikravesh can be used [12], [14]. In turn, the Kik-Piotrowski model can be used to represent the normal force in non-Hertzian contact which considers semi-elliptic normal pressure is considered over the contact patch [15]. Then, the tangential contact forces are determined by considering the contact conditions, namely, the creepages and the normal force applied. Polach has proposed a model to determine the tangential forces that represent the longitudinal, lateral and spin creep effects, being considered elliptic contact patches and the normal distribution of a Hertzian contact [16]. More recently, Piotrowski *et al* have proposed a fast method to determine the creep forces for non-Hertzian contact patches, namely, of the type single double-elliptical contact (SDEC) [17], [18]. According to this approach, the tangential forces are obtained from the interpolation of the Kalker Book of Tables for Non-Hertzian (KBTNH) contact, that has been generated from the software of reference, the CONTACT program.

In this work, a new methodology to implement non-Hertzian contact models in multibody software is presented. A detailed description of this strategy is presented, namely, the wheel and rail surfaces parameterization; the contact detection; the determination of the contact patch and creepages; and the calculation of the normal and tangential forces. Selected case studies have been considered not only to validate the proposed methodology with respect to CONTACT program, but also to compare the computational efficiency with respect to the Hertzian strategy proposed by Pombo *et al* [12].

2

2 Multibody simulation

The dynamic analysis of a multibody system involves the study of its motion and forces transmitted during a given time period, as a function of the initial conditions and operation conditions. In railway applications, the vehicle model as depicted in Fig. 1 is defined by a set of bodies, such as, the carbody, bogie frame and wheelsets which are interconnected by kinematic joints and force elements that represent the vehicle suspension system [4], [5]. The track, considered in this work as rigid, is represented by two databases that describe the position and orientation of the left and right rails as function of their arclength [6], [7]. The vehicle-track interaction is represented by forces developed in the wheel-rail contacting surfaces which are obtained from the wheel-rail contact module [12] described by five tasks listed in Fig. 1. A detailed description of these tasks is presented throughout this paper.
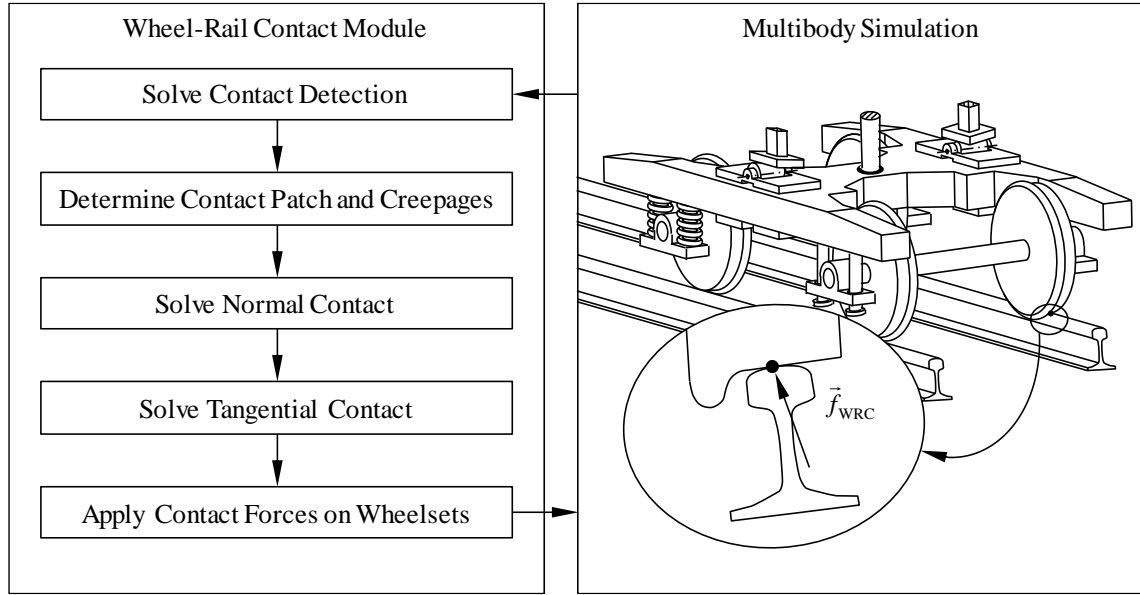

Fig. 1: Wheel-rail contact module of a multibody software

Here, a Cartesian coordinate system is used and all bodies have six degrees of freedom. The governing equations of a railway vehicle system are written as [9]:

$$\begin{bmatrix} \mathbf{M} & \mathbf{\Phi}_\mathbf{q}^\mathrm{T} \\ \mathbf{\Phi}_\mathbf{q} & \mathbf{0} \end{bmatrix} \begin{bmatrix} \ddot{\mathbf{q}} \\ \boldsymbol{\lambda} \end{bmatrix} = \begin{bmatrix} \mathbf{f} \\ \boldsymbol{\gamma} \end{bmatrix} \tag{1}$$

where $\mathbf{M}$ is the mass matrix, $\ddot{\mathbf{q}}$ is the vector of the system accelerations, $\mathbf{f}$ is the force vector, $\mathbf{\Phi}_\mathbf{q}$ is the Jacobian matrix associated with the kinematic constraints, $\boldsymbol{\lambda}$ is the vector of Lagrange multipliers, which are related to the joint reaction forces and $\boldsymbol{\gamma}$ is the right-hand side of the acceleration constraint equations. The forces developed in the contacting surfaces, represented in Fig. 1 by the vector $\mathbf{f}_{\mathrm{WRC}}$, are included in term $\mathbf{f}$ as external forces.

3 Wheel and rail surface parameterization

Since the forces developed in the contacting surfaces depend on the wheel-rail interference, the parameterization of the wheel and rail surfaces is required, namely, the position, tangent and normal vectors, and surface curvatures at any point of the surface must be defined. Note that, in the formulation presented throughout this paper, the superscripts 'L' and 'R' refer to the left and right side, respectively, while the superscript '*side*' is used when generalization is possible. This is important to identify formulation for the left and right wheel and rail.

3

The wheel surface is obtained by the revolution of the wheel cross-section represented in Fig. 2(a) around its axis. In turn, the rail surface is described by the sweep of the rail cross-section shown in Fig. 2(b) along the rail path which is described by a database that comprises a set of nodal points as listed in Tab. 1. Each nodal point contains the position and orientation of the rail as function of s_r^{side} which is a coordinate that defines the rail arclength, as shown in Fig. 3. The position of the rail profile origin is given by $\mathbf{r}_r^{side} = \left[r_x^{side}, r_y^{side}, r_z^{side} \right]$; the unitary vector perpendicular vector to the rail cross-section is defined by $\mathbf{t}_r^{side} = \left[t_x^{side}, t_y^{side}, t_z^{side} \right]$, the unitary vector $\mathbf{n}_r^{side} = \left[n_x^{side}, n_y^{side}, n_z^{side} \right]$ corresponds to the transversal coordinate u_r, while the unitary vector $\mathbf{b}_r^{side} = \left[b_x^{side}, b_y^{side}, b_z^{side} \right]$ defines the vertical coordinate f_r, as shown in Fig. 2(b). Note that, the subscripts '1' and 'end' refer to the first and last nodal point, respectively, while 'j' refers to a generic nodal point of the rail database. This database is obtained from the pre-processor tool that uses the track design geometry, namely, the curvature and cant angle, and its track irregularities [6], [7]. Thus, the linear interpolation at s_r^{side} lead to the position and orientation of the rail profile at such arclength.

Once the wheel and rail cross-sections are specified by a set of nodal points as shown in Fig. 2, the interpolation of these information is considered to provide a continuous description of the wheel and rail surfaces. Since the position, tangent and normal vectors, and the curvature at any point of the surfaces are required, the profiles are interpolated by cubic splines [12].
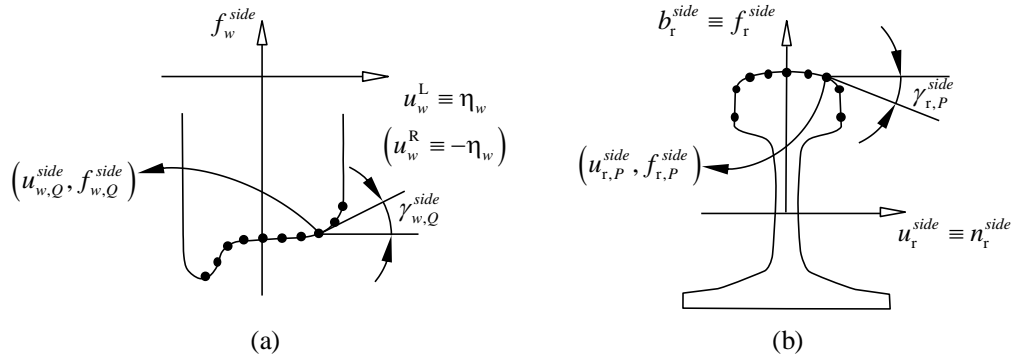

Fig. 2: (a) Wheel and (b) rail profiles defined by a set of nodal points

$s_{r,1}^{side}$	$r_{x,1}^{side}$	$r_{y,1}^{side}$	$r_{z,1}^{side}$	$t_{x,1}^{side}$	$t_{y,1}^{side}$	$t_{z,1}^{side}$	$n_{x,1}^{side}$	$n_{y,1}^{side}$	$n_{z,1}^{side}$	$b_{x,1}^{side}$	$b_{y,1}^{side}$	$b_{z,1}^{side}$
$\vdots$	$\vdots$	$\vdots$	$\vdots$	$\vdots$	$\vdots$	$\vdots$	$\vdots$	$\vdots$	$\vdots$	$\vdots$	$\vdots$	$\vdots$
$s_{r,j}^{side}$	$r_{x,j}^{side}$	$r_{y,j}^{side}$	$r_{z,j}^{side}$	$t_{x,j}^{side}$	$t_{y,j}^{side}$	$t_{z,j}^{side}$	$n_{x,j}^{side}$	$n_{y,j}^{side}$	$n_{z,j}^{side}$	$b_{x,j}^{side}$	$b_{y,j}^{side}$	$b_{z,j}^{side}$
$\vdots$	$\vdots$	$\vdots$	$\vdots$	$\vdots$	$\vdots$	$\vdots$	$\vdots$	$\vdots$	$\vdots$	$\vdots$	$\vdots$	$\vdots$
$s_{r,end}^{side}$	$r_{x,end}^{side}$	$r_{y,end}^{side}$	$r_{z,end}^{side}$	$t_{x,end}^{side}$	$t_{y,end}^{side}$	$t_{z,end}^{side}$	$n_{x,end}^{side}$	$n_{y,end}^{side}$	$n_{z,end}^{side}$	$b_{x,end}^{side}$	$b_{y,end}^{side}$	$b_{z,end}^{side}$

Tab. 1: Rail database that defines its position and orientation as function of its arclength

The position of point Q in the left or in the right wheel surface of wheelset w, that is, the vectors $\mathbf{r}_Q^L$ and $\mathbf{r}_Q^R$ shown in Fig. 3, can be written as:

$$\mathbf{r}_Q^{side} = \mathbf{r}_w + \mathbf{r}_w^{side} + \mathbf{r}_{w,Q}^{side} \tag{2}$$

where $\mathbf{r}_w$ is the position vector of the wheelset w, $\mathbf{r}_w^{side}$ defines the distance between the wheelset centre of gravity and the wheel profile origin, and $\mathbf{r}_{w,Q}^{side}$ defines the distance between the wheel origin profile and the point Q, as shown in Fig. 3. The vector $\mathbf{r}_w^{side}$ can be written as:

$$\mathbf{r}_w^L = \mathbf{A}_w \begin{bmatrix} 0 & H/2 & 0 \end{bmatrix}^T \quad , \quad \mathbf{r}_w^R = \mathbf{A}_w \begin{bmatrix} 0 & -H/2 & 0 \end{bmatrix}^T \tag{3}$$

4

where $\mathbf{A}_w$ is the transformation matrix of the wheelset w that also defines the local reference frame attached to the wheelset $(\xi_w/\eta_w/\zeta_w)$ as depicted in Fig. 3, and H is the distance between the wheel profiles. The vector $\mathbf{r}_{w,Q}^{side}$ is defined as:

$$\mathbf{r}_{w,Q}^{side} = \mathbf{A}_w \mathbf{A}_w^{side} \begin{bmatrix} 0 & u_{w,Q}^{side} & f_{w,Q}^{side} \end{bmatrix}^{\mathrm{T}} \tag{4}$$

where $\left(u_{w,Q}^{side}, f_{w,Q}^{side} \right)$ is the point Q measured with respect to the two-dimensional reference frame $\left(u_w^{side} / f_w^{side} \right)$ as shown in Fig. 2(a). the matrix $\mathbf{A}_w^{side}$ is defined by

$$\mathbf{A}_w^{\mathrm{L}} = \begin{bmatrix} \cos\left(s_{w,Q}^{\mathrm{L}}\right) & 0 & \sin\left(s_{w,Q}^{\mathrm{L}}\right) \\ 0 & 1 & 0 \\ -\sin\left(s_{w,Q}^{\mathrm{L}}\right) & 0 & \cos\left(s_{w,Q}^{\mathrm{L}}\right) \end{bmatrix} \quad , \quad \mathbf{A}_w^{\mathrm{R}} = \begin{bmatrix} -\cos\left(s_{w,Q}^{\mathrm{R}}\right) & 0 & -\sin\left(s_{w,Q}^{\mathrm{R}}\right) \\ 0 & -1 & 0 \\ -\sin\left(s_{w,Q}^{\mathrm{R}}\right) & 0 & \cos\left(s_{w,Q}^{\mathrm{R}}\right) \end{bmatrix} \tag{5}$$

where $s_{w,Q}^{\mathrm{L}}$ and $s_{w,Q}^{\mathrm{R}}$ are the angular coordinates of each wheel shown in Fig. 3. Thus, the two parameters $s_{w,Q}^{side}$ and $u_{w,Q}^{side}$ define any point of the wheel surface.
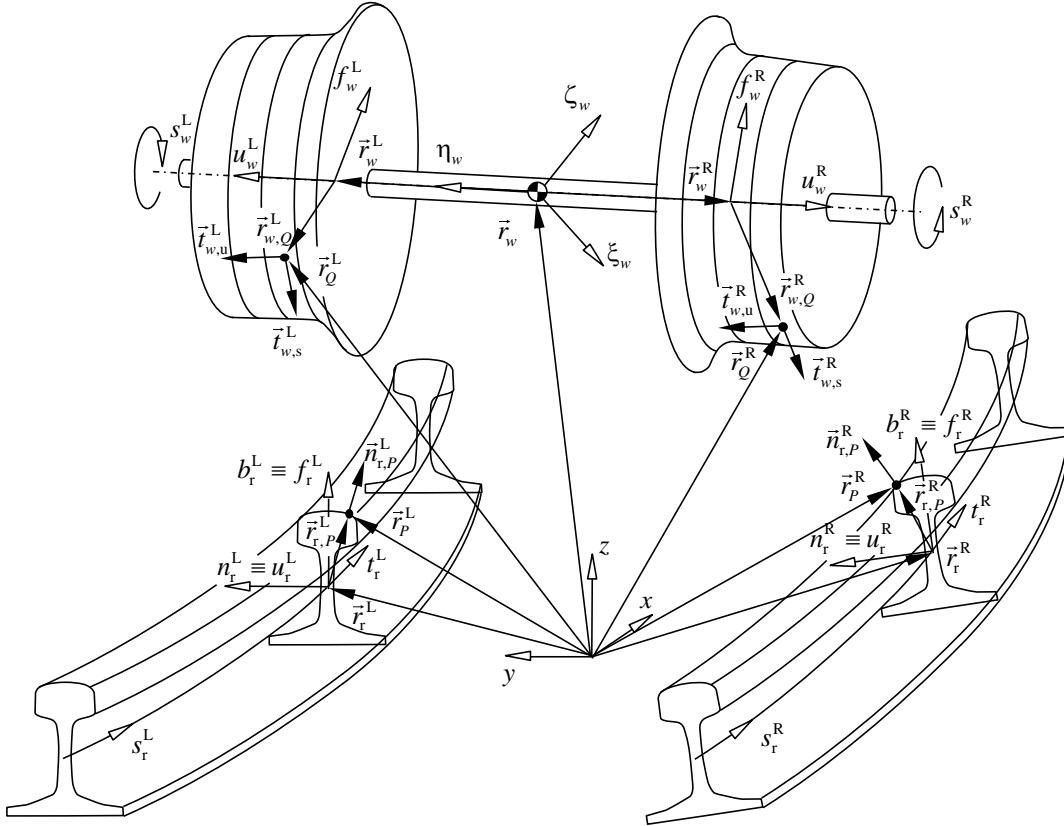

Fig. 3: Parameterization of the wheel and rail surfaces

For the wheel, two vectors tangent to the wheel surface must be defined. Here, the tangent vectors $\mathbf{t}_{w,s}^{side}$ and $\mathbf{t}_{w,u}^{side}$ depicted in Fig. 3 are considered. The tangent vectors parallel to the rolling motion of the left and right wheels are defined as:

$$\mathbf{t}_{w,s}^{\mathrm{L}} = \mathbf{A}_w \mathbf{A}_w^{\mathrm{L}} \begin{bmatrix} 1 & 0 & 0 \end{bmatrix}^{\mathrm{T}} \quad , \quad \mathbf{t}_{w,s}^{\mathrm{R}} = \mathbf{A}_w \mathbf{A}_w^{\mathrm{R}} \begin{bmatrix} -1 & 0 & 0 \end{bmatrix}^{\mathrm{T}} \tag{6}$$

while the transversal tangent vectors are defined as:

5

$$\mathbf{t}_{w,u}^{side} = \mathbf{A}_w \mathbf{A}_w^{side} \begin{bmatrix} 0 & \cos\left(\gamma_{w,Q}^{side}\right) & \sin\left(\gamma_{w,Q}^{side}\right) \end{bmatrix}^T \tag{7}$$

where $\gamma_{w,Q}^{side}$ is the angle shown in Fig. 2(a) that can be determined by:

$$\gamma_{w,Q}^{side} = \tan^{-1}\left(\frac{df_w^{side}\left(u_{w,Q}^{side}\right)}{du_w^{side}}\right) \tag{8}$$

The curvature of the wheel in the longitudinal direction is defined by:

$$\kappa_{w,s}^{side} = \frac{1}{f_w^{side}\left(u_{w,Q}^{side}\right)\sqrt{1+\left(\frac{df_w^{side}\left(u_{w,Q}^{side}\right)}{du_w^{side}}\right)^2}} \tag{9}$$

while in the transversal direction is obtained as:

$$\kappa_{w,u}^{side} = \left|\frac{d^2 f_{w,u}^{side}\left(u_{w,Q}^{side}\right)}{du_w^{side\,2}} \middle/ \left[1+\left(\frac{df_w^{side}\left(u_{w,Q}^{side}\right)}{du_w^{side}}\right)^2\right]^{3/2}\right| \tag{10}$$

The position of point P in a rail surface is written as:

$$\mathbf{r}_P^{side} = \mathbf{r}_r^{side} + \mathbf{r}_{r,P}^{side} \tag{11}$$

where $\mathbf{r}_r^{side}$ defines the position vector of the rail profile for a given s_r^{side}, which is interpolated from the rail database, and $\mathbf{r}_{r,P}^{side}$ is the distance between the rail profile origin and the point P of the rail, as shown in Fig. 3, is defined as:

$$\mathbf{r}_{r,P}^{side} = \mathbf{A}_r^{side} \begin{bmatrix} 0 & u_{r,P}^{side} & f_{r,P}^{side} \end{bmatrix}^T \tag{12}$$

where $\left(u_{r,P}^{side}, f_{r,P}^{side}\right)$ is the position of point P measured in the profile reference frame $\left(u_r^{side}/f_r^{side}\right)$ as indicated in Fig. 2(b), and matrix $\mathbf{A}_w^{side}$ the local reference frame of the profile $\left(t_r^{side}/n_r^{side}/b_r^{side}\right)$ as depicted in Fig. 3 These unitary vectors are the tangent, normal and binormal vectors of the rail at s_r which are obtained from the interpolation of the databases

$$\mathbf{n}_r^{side} = \mathbf{A}_r^{side} \begin{bmatrix} 0 & -\sin\left(\gamma_{r,P}^{side}\right) & \cos\left(\gamma_{r,P}^{side}\right) \end{bmatrix}^T \tag{13}$$

where $\gamma_{r,P}^{side}$ is the angle shown in Fig. 2(b) that can be determined by:

$$\gamma_{r,P}^{side} = \tan^{-1}\left(\frac{df_r^{side}\left(u_{r,P}^{side}\right)}{du_r^{side}}\right) \tag{14}$$

The curvature of the rail in the longitudinal direction is defined by:

$$\kappa_{r,s}^{side} = 0 \tag{15}$$

while in the transversal direction is obtained as:

6

$$\kappa_{r,u}^{side} = \left| \frac{d^2 f_r^{side}\left(u_{r,P}^{side}\right)}{d\left(u_r^{side}\right)^2} \middle/ \left[1 + \left(\frac{df_r^{side}\left(u_{r,P}^{side}\right)}{du_r^{side}} \right)^2 \right]^{3/2} \right| \qquad (16)$$

Note that the assumption $\kappa_{r,s}^{side} = 0$ is only valid since the track slope is negligible.

4   Surfaces interaction

4.1   Contact detection

For the wheel-rail contact models considered in this work, forces are transmitted between surface if virtual penetration occurs. For the contact detection problem, four vectors are considered, namely, the tangent vectors $\mathbf{t}_{w,s}^{side}$ and $\mathbf{t}_{w,u}^{side}$, the normal vector $\mathbf{n}_r^{side}$, and the distance vector $\mathbf{d}$ written as:

$$\mathbf{d}^{side} = \mathbf{r}_P^{side} - \mathbf{r}_Q^{side} \qquad (17)$$

where points Q and P are defined by the parameters ($s_{w,Q}^{side}, u_{w,Q}^{side}$) and ($s_{r,P}^{side}, u_{r,Q}^{side}$), respectively, as shown in Fig. 4(a). At non-conformal conditions, that is, when the contacting surfaces are convex, the contact detection problem consist of solving the system of four non-linear equations written as [12]:

$$\mathbf{f}_{nl}\left(s_{w,Q}^{side}, u_{w,Q}^{side}, s_{r,P}^{side}, u_{r,P}^{side}\right) = \mathbf{0} \Leftrightarrow \begin{cases} \left(\mathbf{n}_r^{side}\right)^T \mathbf{t}_{w,s} = 0 \\ \left(\mathbf{n}_r^{side}\right)^T \mathbf{t}_{w,u} = 0 \\ \left(\mathbf{d}_r^{side}\right)^T \mathbf{t}_{w,s} = 0 \\ \left(\mathbf{d}_r^{side}\right)^T \mathbf{t}_{w,u} = 0 \end{cases} \qquad (18)$$

The solution of this problem defines two potential points of contact in the wheel and rail, being ensured that the vectors $\mathbf{n}_r^{side}$ and $\mathbf{d}^{side}$ are colinear and perpendicular to the vectors $\mathbf{t}_{w,s}^{side}$ and $\mathbf{t}_{w,u}^{side}$. To verify that the contact between the wheel and rail exists, it is assessed the direction of vectors $\mathbf{n}_r^{side}$ and $\mathbf{d}^{side}$, as shown in Fig. 4(b). If the $\mathbf{n}_r^{side^T} \mathbf{d}^{side} > 0$, then the surfaces are in contact, otherwise, no contact are transmitted between the surfaces. Note that the interaction between the wheel and rail at the tread-flange transition must be neglected since here the non-conformality assumption is not valid, that is, no solution exists for the problem defined by expression (18) Thus, two profiles are considered to describe the wheel profile, one that represents the tread and another to represent the flange, being possible only two points of contact for the wheel-rail interaction.

4.2   Contact patch

When Hertzian contact is considered, the contact patch is assumed to be an ellipse that can be defined by the semi-axis [12]:

$$a = m\sqrt[3]{\frac{3\pi}{4} \frac{h_w + h_r}{A + B} N} \quad , \quad b = n\sqrt[3]{\frac{3\pi}{4} \frac{h_w + h_r}{A + B} N} \qquad (19)$$

where m and n are tabulated values [12]; h_w and h_r are material parameters of the wheel and rail, respectively; N is the normal contact force; and A and B are the curvatures written as:

$$A = \frac{1}{2}\left(\kappa_{r,u}^{side} + \kappa_{w,u}^{side}\right) \quad , \quad B = \frac{1}{2}\left(\kappa_{r,s}^{side} + \kappa_{w,s}^{side}\right) \qquad (20)$$

where curvatures $\kappa_{w,s}^{side}$, $\kappa_{w,u}^{side}$, $\kappa_{r,s}^{side}$, and $\kappa_{r,u}^{side}$ are determined by expressions (9), (10), (15) and (16), respectively.
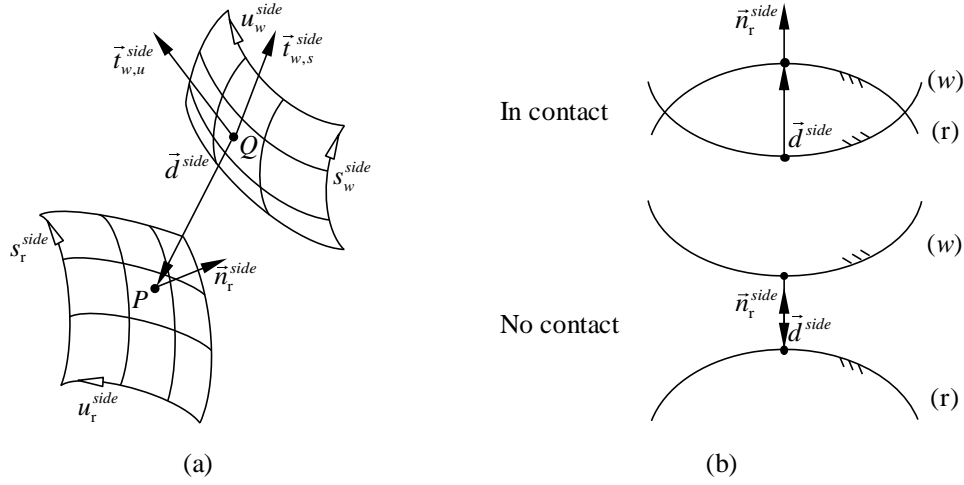

Fig. 4: (a) Vectors used for the contact detection between two surfaces and (b) the 'in contact' and 'no contact' configurations

In the non-Hertzian contact case, the undeformed distance function must be calculated to determine the contact patch. This requires the definition of the wheel and rail profiles with respect to the contact patch reference frame defined here by $\left(x_{cp}^{side} \;/\; y_{cp}^{side} \;/\; g_{cp}^{side} \right)$ whose origin is the point of contact in the wheel, as shown in Fig. 5, in which $x_{cp}^{side} \equiv \mathbf{t}_{w,s}^{side}$, $y_{cp}^{side} \equiv \mathbf{t}_{w,u}^{side}$ and $g_{cp}^{side} \equiv \mathbf{n}_{r}^{side}$. Note that only part of the wheel and rail profiles must be considered, namely, the region where virtual penetration occurs. Fig. 5 shows dots that represent the discrete domain of the wheel and rail cross-section in which the contact occurs, while the crosses represent points where no interference occurs being out of the domain of interest. The domain of axis y_{cp}^{side} is defined by a specified equal spacing of Δy in which $y_{cp,i}^{side} = 0$ is included in the domain. Moreover, because the wheel and rail profiles are projected onto the plane $\left(y_{cp}^{side} \;/\; g_{cp}^{side} \right)$, the coordinate x_{cp}^{side} is null for any point of the undeformed distance function.
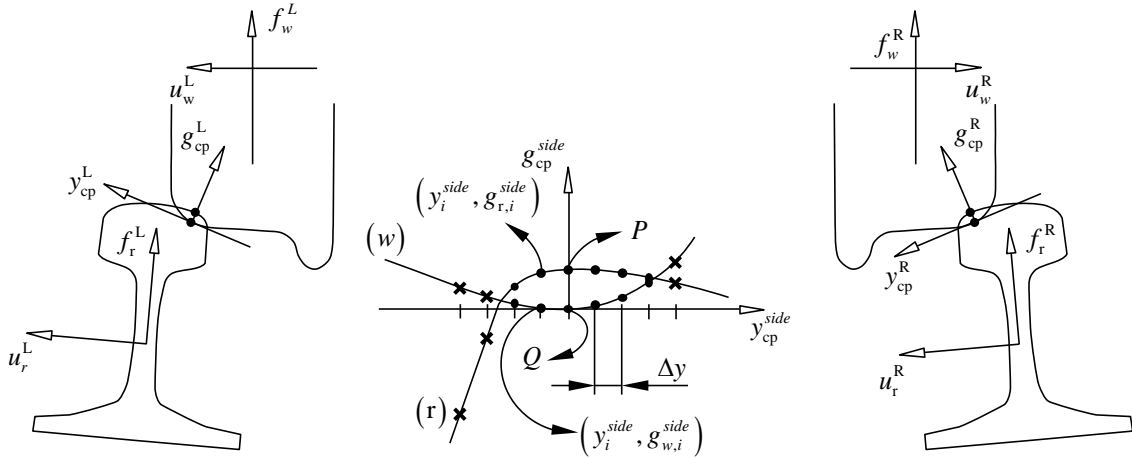

Fig. 5: Definition of the wheel and rail profile in the contact patch reference frame

The points Q and P, in the reference frame $\left(y_{cp}^{side} \;/\; g_{cp}^{side} \right)$, are defined as $Q \equiv (0,0)$ and $P \equiv (0, \delta^{side})$, where δ^{side} is the maximum penetration determined as:

$$\delta^{side} = \sqrt{\left(\mathbf{d}^{side} \right)^{\mathrm{T}} \mathbf{d}^{side}} \tag{21}$$

8

However, to determine the coordinates from another point of the wheel and rail, namely, at $y_{cp}^{side} = y_i^{side} \neq 0$, a transformation from the profile reference frame to the contact patch reference frame is required. For the wheel, the position vector of a point of the surface can be defined by the two alternatives:

$$\mathbf{r}_{w,y}^{side} = \mathbf{r}_w + \mathbf{r}_w^{side} + \mathbf{r}_{w,y}^{side}$$

$$\mathbf{r}_{w,y}^{side} = \mathbf{r}_w + \mathbf{r}_w^{side} + \mathbf{r}_{w,Q}^{side} + \mathbf{A}_{cp}^{side} \begin{bmatrix} 0 & y_i^{side} & g_{w,i}^{side} \end{bmatrix}^T \tag{22}$$

where the relation of these equations lead to:

$$\begin{bmatrix} 0 & y_i^{side} & g_{w,i}^{side} \end{bmatrix}^T = \mathbf{B}^{side} \begin{bmatrix} 0 & \left(u_{w,y}^{side} - u_{w,Q}^{side} \right) & \left(f_{w,y}^{side} - f_{w,Q}^{side} \right) \end{bmatrix}^T \tag{23}$$

where:

$$\mathbf{B}^{side} = \left[\mathbf{A}_{cp}^{side} \right]^{-1} \mathbf{A}_w \mathbf{A}_w^{side} \tag{24}$$

being $\mathbf{A}_{cp}^{side} = \begin{bmatrix} \mathbf{t}_{w,s}^{side} & \mathbf{t}_{w,u}^{side} & \mathbf{n}_r^{side} \end{bmatrix}$. Note that the pair $\left(u_{w,y}^{side}, f_{w,y}^{side} \right)$ must be determined by solving the non-linear equation written as:

$$B_{(2,2)}^{side} \left(u_{w,y}^{side} - u_{w,Q}^{side} \right) + B_{(2,3)}^{side} \left(f_{w,y}^{side} - f_{w,Q}^{side} \right) - y_{w,i}^{side} = 0 \tag{25}$$

where $u_{w,y}^{side}$ is the only unknown since $f_{w,y}^{side} \equiv f\left(u_{w,y}^{side} \right)$. Then, the ordinate of the wheel point at y_i^{side} is defined as:

$$g_{w,i}^{side} = B_{(3,2)}^{side} \left(u_{w,y}^{side} - u_{w,Q}^{side} \right) + B_{(3,3)}^{side} \left(f_{w,y}^{side} - f_{w,Q}^{side} \right) \tag{26}$$

For the rail, the same procedure presented above is followed. In this case, the two alternatives to define the position of a point of the rail at $y_{cp}^{side} = y_i^{side}$ are:

$$\mathbf{r}_{r,y}^{side} = \mathbf{r}_r^{side} + \mathbf{r}_{r,y}^{side}$$

$$\mathbf{r}_{r,y}^{side} = \mathbf{r}_r^{side} + \mathbf{r}_{r,P}^{side} + \mathbf{A}_{cp}^{side} \begin{bmatrix} 0 & y_{r,i}^{side} & g_{r,i}^{side} - \delta \end{bmatrix}^T \tag{27}$$

where the relation of these equations leads to:

$$\begin{bmatrix} 0 & y_{r,i}^{side} & g_{r,i}^{side} \end{bmatrix}^T = \mathbf{B}^{side} \begin{bmatrix} 0 & \left(u_{r,y}^{side} - u_{r,P}^{side} \right) & \left(f_{r,y}^{side} - f_{r,P}^{side} \right) \end{bmatrix}^T + \begin{bmatrix} 0 & 0 & \delta^{side} \end{bmatrix}^T \tag{28}$$

The parameters $u_{r,i}^{side}$ is obtained by solving the non-linear equation written as:

$$B_{(2,2)}^{side} \left(u_{r,y}^{side} - u_{r,P}^{side} \right) + B_{(2,3)}^{side} \left(f_{r,y}^{side} - f_{r,P}^{side} \right) - y_{r,i}^{side} = 0 \tag{29}$$

and hence the ordinate of the rail point is defined as:

$$g_{r,i}^{side} = B_{(3,2)}^{side} \left(u_{r,y}^{side} - u_{r,P}^{side} \right) + B_{(3,3)}^{side} \left(f_{r,y}^{side} - f_{r,P}^{side} \right) + \delta^{side} \tag{30}$$

Once both profiles are defined with respect to the contact patch reference frame, the undeformed distance function is obtained as:

$$g_{und}^{side}(y) = g_w^{side}(y) - g_r^{side}(y) + \delta \tag{31}$$

Fig. 6(a) shows an illustration of an undeformed distance function. Thus, the contact patch can be determined being the positive edge of the contact patch defined as [15]:

9

$$x_{\mathrm{L}}(y) = \sqrt{2R\left(\varepsilon\delta - g_{und}^{side}(y)\right)} \tag{32}$$

where ε is considered equal to 0.55 to take into account the existing deformation of the contacting surfaces [15] and R_Q is the radius at the contact patch in the rolling direction in point Q, written as:

$$R_Q = -f_{w,Q}^{side}\sqrt{1+\left(\frac{df_{w,Q}^{side}}{du_w}\right)^2} \tag{33}$$

Note that the contact patch consists of a set of strips, being the contact patch symmetric with respect to the y_{cp}^{side} axis, as shown in Fig. 6(b).
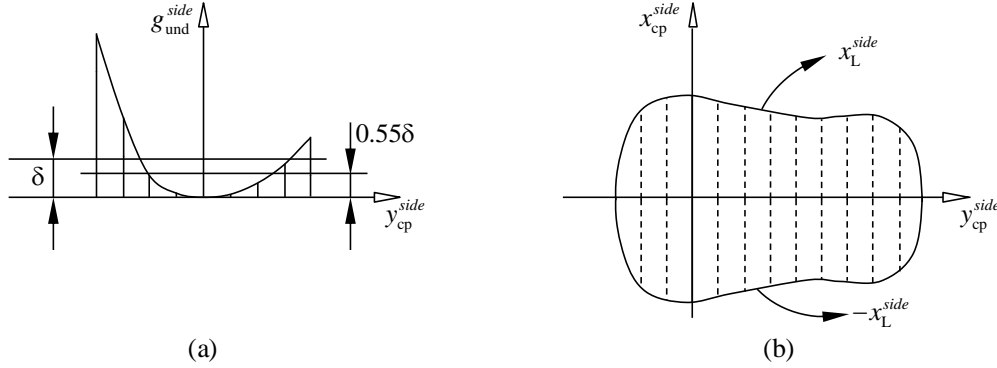

(a)   (b)

Fig. 6: (a) Undeformed distance function and (b) contact patch

4.3   Creepages

Once the contacting patch area is identified, a kinematic analysis at this region lead to the determination of the longitudinal, lateral and spin creepages, defined as:

$$\upsilon_x = \frac{\mathbf{v}_{rel}^{\mathrm{T}}\mathbf{t}_{w,s}}{V_w} \tag{34}$$

$$\upsilon_y = \frac{\mathbf{v}_{rel}^{\mathrm{T}}\mathbf{t}_{w,u}}{V_w} \tag{35}$$

$$\varphi = \frac{\boldsymbol{\omega}_w^{\mathrm{T}}\mathbf{n}_{\mathrm{r}}}{V_w} \tag{36}$$

where V_w is the speed of the wheelset w, $\boldsymbol{\omega}_w$ is the angular speed vector of the wheelset w, and $\mathbf{v}_{rel}$ is the relative speed at the contacting points defined as:

$$\mathbf{v}_{rel} = \mathbf{v}_Q - \mathbf{v}_P \tag{37}$$

where $\mathbf{v}_P$ is null since the track is considered rigid, and:

$$\mathbf{v}_Q = \mathbf{v}_w + \boldsymbol{\omega}_w\left(\mathbf{r}_w^{side} + \mathbf{r}_{w,Q}^{side}\right) \tag{38}$$

where $\boldsymbol{\omega}_w$ is the angular speed vector of wheelset w.

10

5   Normal contact

5.1   Lankarani-Nikravesh model

In this work, the normal contact force model proposed by Lankarani and Nikravesh is used when the Hertzian strategy is considered [12]. This consists of a Hertzian contact with hysteresis damping, being defined as [14]:

$$N^{\mathrm{LN}} = K\delta^n \left(1 + \frac{3\left(1-e^2\right)}{4} \frac{\dot{\delta}}{\dot{\delta}^{(-)}} \right) \tag{39}$$

where K is the stiffness coefficient, n is equal to 1.5 for metals, e is the restitution coefficient, $\dot{\delta}$ is the first time derivative of δ and $\dot{\delta}^{(-)}$ is defined as the maximum value $\dot{\delta}$ during the contact such that the ratio $\dot{\delta}/\dot{\delta}^{(-)}$ is lower or equal to 1 [12].

5.2   Kik-Piotrowski model

For the non-Hertzian contact, the normal contact pressure proposed by Kik and Piotrowski is used [15]. In this model, semi-elliptic normal pressure distribution in the rolling direction is considered, as depicted in Fig. 7(a). The normal pressure distribution in the contact patch is defined as [15]:

$$p\left(x,y\right) = \frac{p_0}{x_{\mathrm{L}}\left(y=0\right)} \sqrt{x_L^2\left(y\right)-x^2} \tag{40}$$

where p_0 is the maximum normal pressure. Since during the multibody simulation p_0 is not known, the assumption proposed in the Kik-Piotrowski model estimates the maximum pressure as [15]:

$$p_0 = \frac{\pi E \delta x_{\mathrm{L}}\left(y=0\right)}{2\left(1-\sigma^2\right)} \left[\sum_{i=1}^{n_y} \left(\int_{-x_{\mathrm{L}}(y)}^{x_{\mathrm{L}}(y)} f_{\mathrm{B}}\left(x,y\right)dx \right)\Delta y \right]^{-1} \tag{41}$$

where n_y is the number of strips that define the contact patch, E and σ are the Young modulus and Poisson ratio of the wheel and rail, respectively, and the function to be integrated is defined as [15]:

$$f_{\mathrm{B}}\left(x,y\right) = \frac{\sqrt{x_L^2\left(y\right)-x^2}}{\sqrt{x^2+y^2}} \tag{42}$$

Note that the integration in direction y is simplified since the contact patch is defined by strips. Special attention is put in the integration of the function $f_{\mathrm{B}}(x,y)$, namely, for the strip at $y=0$. In this case, this function tends to infinity, that is, $f_{\mathrm{B}}(0,0)=\infty$ and hence p_0 tend to zero. Since the trapezoidal rule is used for fast integral calculation, point $x=0$ is not considered, being the domain of axis x_{cp} defined as shown in Fig. 7(b). Note that, for other strip, that is, for $y_i{\neq}0$, the function $f_{\mathrm{B}}(x,0)$ do not exhibit any numerical problem as shown in Fig. 7(b). Thus, the normal contacting force results from [15]:

$$N^{\mathrm{KP}} = \sum_{i=1}^{n_y} \left(\int_{-x_{\mathrm{L}}(y)}^{x_{\mathrm{L}}(y)} p\left(x,y\right)dx \right)\Delta y \tag{43}$$

The step size considered for the integration in the x direction of Δy in order to consider the same refinement in the lateral direction.
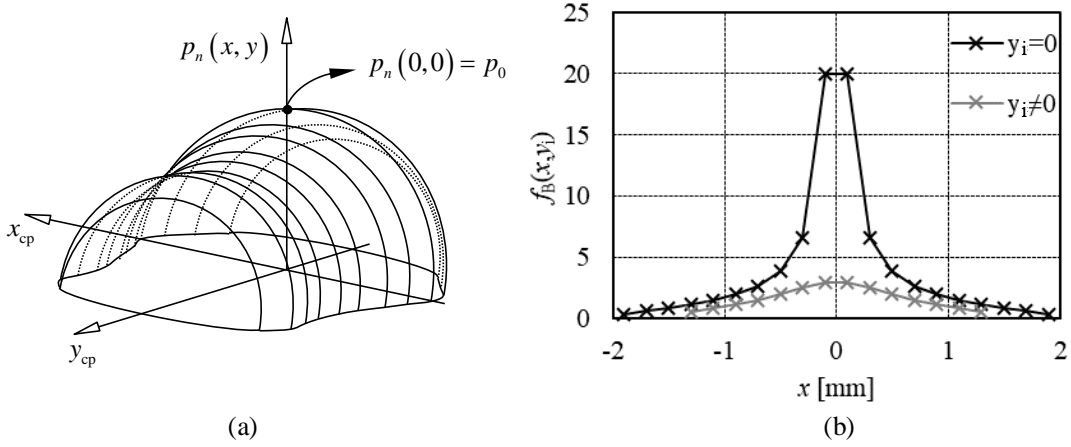
Fig. 7: (a) Normal pressure distribution of the KP model and (b) function $f_B(x,y)$ for the central strip $y_i=0$ and other $y_i\neq0$

6 Tangential contact

6.1 Polach model

For Hertzian contact the Polach model is used to determine the longitudinal and lateral creepages, being the ignored the spin creep moment [16]. These forces are defined as:

$$F_x^{\text{Polach}} = F\frac{\upsilon_x}{\upsilon_C} \quad , \quad F_y^{\text{Polach}} = F\frac{\upsilon_y}{\upsilon_C} + F_{\eta S}\frac{\varphi}{\upsilon_C} \quad , \quad M_z^{\text{Polach}} = 0 \tag{44}$$

where F is the tangential contact force caused by longitudinal and lateral creepages, υ_C is the modified translational creepage, which accounts the effect of spin creepage, and $F_{\eta S}$ is the lateral tangential force caused by spin creepage

6.2 KBTNH model

For the non-Hertzian methodology, the so-called Kalker Book of Tables for Non-Hertzian contact proposed by Piotrowski *et al* is used in this work [17], [18]. This model approximates the non-Hertzian contact patch to a single double-elliptical contact as shown in Fig. 8. To interpolate the KBTNH and hence to obtain the tangential contact forces, five regularized inputs must be determined. Three are related to the creepages being written as:

$$\xi = \frac{\rho\upsilon_x}{\mu c} \quad , \quad \eta = \frac{\rho\upsilon_y}{\mu c} \quad , \quad \chi = \frac{\rho\varphi}{\mu} \tag{45}$$

where ρ is a characteristic length of the elliptical contact patch, μ is friction coefficient and $c = \sqrt{ab}$ [17], [18]. For convenience, the regularized creepages ξ and η are alternatively defined by:

$$v = \sqrt{\xi^2 + \eta^2} \quad , \quad \alpha = \tan^{-1}\left(\frac{\eta}{\xi}\right) \tag{46}$$

that is, the translational creep magnitude and its directional angle with respect to the rolling direction, respectively. Then, two regularised geometrical parameters are considered, namely:

$$g = \frac{a}{b} \quad , \quad \psi = \frac{y_0}{b} \tag{47}$$

where a, b and y_0 are the dimensions of the simple double-elliptical contact (SDEC) shape as shown in Fig. 8(b). To obtain such dimension the following relations are used:

$$a = \sqrt{\frac{A}{\pi}\frac{(W_1 + W_2)}{W_3}} \quad , \quad b = \sqrt{\frac{A}{\pi}\frac{W_3}{(W_1 + W_2)}} \quad , \quad y_0 = b\frac{W_1 - W_2}{W_3} \tag{48}$$

where A is the area of the contact patch, and W_1, W_2 and W_3 are the dimensions depicted in Fig. 8(a). The outputs of the KBTNH, that is, the regularised forces f_x, f_y and m_z are obtained from linear interpolation of the pre-calculated lookup table. The creep forces are obtained as:

$$F_x^{KBTNH} = \mu N f_x \quad , \quad F_y^{KBTNH} = \mu N f_y \quad , \quad M_z^{KBTNH} = \mu c N m_z \tag{49}$$

The discretization and the number of point considered for each input of the KBTNH are listed in Tab. 2. Note that α only covers the domain $[-\pi/2; \pi/2]$, while only positive values of χ are considered. To determine contact forces for other cases not comprised in the KBTNH domain, the symmetries listed in Tab. 3 are used. The right column of this table represents the domain described in Tab. 2. In each cell, it is described not only the domain in terms of ξ, η, χ and ψ, but also the outputs of the lookup table. For example, for a set of inputs that fits in the conditions $\xi<0$, $\eta\geq0$, $\chi<0$ and $\psi\geq0$, which is defined by the cell in the top left, the outputs are obtained based on the ones listed in the cell in the right column in 3rd row, that is, $f_x = -f_x^3$, $f_y = -f_y^3$ and $m_z = -m_z^3$.
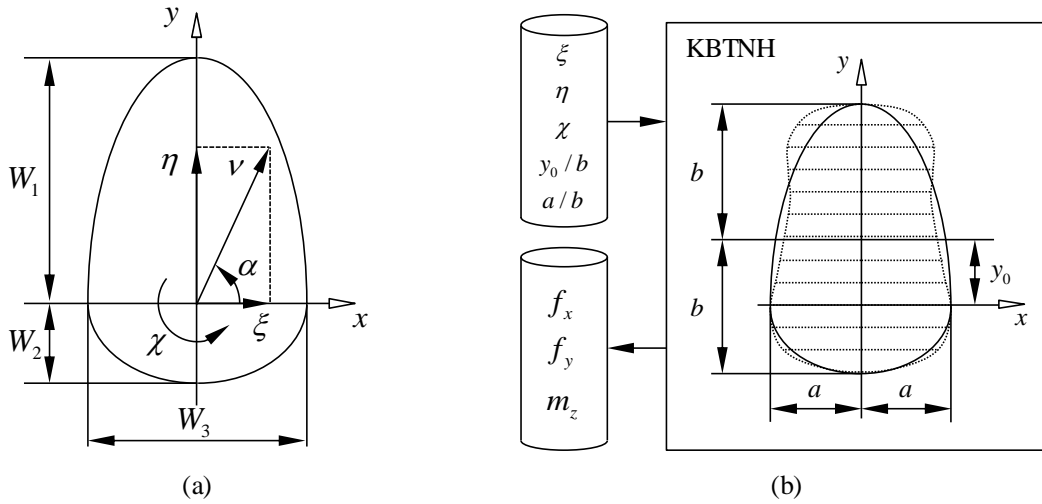

Fig. 8: (a) Simple double-elliptical contact (SDEC) patch and creepages, and (b) input and output of the KBTNH

	n_g=8
$g = \left\{\dfrac{1}{5} \quad \dfrac{1}{2} \quad \dfrac{3}{4} \quad 1 \quad 2 \quad 3 \quad 4 \quad 5\right\}$	
$\alpha = \left\{-\dfrac{\pi}{2} \quad -\dfrac{\pi}{3} \quad -\dfrac{\pi}{6} \quad 0 \quad \dfrac{\pi}{6} \quad \dfrac{\pi}{3} \quad \dfrac{\pi}{2}\right\}$	n_α=7
$\chi = \{0.00 \quad 0.25 \quad 0.50 \quad 1.00 \quad 1.25 \quad 1.50 \quad 1.75 \quad 2.00\}$	n_χ=8
$v = \{0.0 \quad 0.1 \quad 0.2 \quad 0.3 \quad 0.4 \quad 0.5 \quad 0.7 \quad 0.9 \quad 1.1 \quad 1.4 \quad 1.7 \quad 2.0$ $\quad 2.5 \quad 3.0 \quad 3.5 \quad 4.0 \quad 5.0 \quad 6.0 \quad 7.0 \quad 8.0 \quad 9.0 \quad 10.0 \quad 12.0\}$	n_v=23
$\psi = \{-0.9 \quad -0.8 \quad -0.6 \quad -0.4 \quad -0.2 \quad 0.0 \quad 0.2 \quad 0.4 \quad 0.6 \quad 0.8 \quad 0.9\}$	n_ψ=11

Tab. 2: Domain of the Kalker Book of Tables for Non-Hertzian (KBTNH) contact [17], [18]

$\xi<0$ $\quad\chi<0$ $\eta\geq0$ $\quad\psi\geq0$ $-f_x^3$ $\quad-f_y^3$ $\quad-m_z^3$	$\xi<0$ $\quad\chi\geq0$ $\eta\geq0$ $\quad\psi\geq0$ $-f_x^2$ $\quad f_y^2$ $\quad m_z^2$	$\xi\geq0$ $\quad\chi<0$ $\eta\geq0$ $\quad\psi\geq0$ f_x^4 $\quad-f_y^4$ $\quad-m_z^4$	$\xi\geq0$ $\quad\chi\geq0$ $\eta\geq0$ $\quad\psi\geq0$ f_x^1 $\quad f_y^1$ $\quad m_z^1$
$\xi<0$ $\quad\chi<0$ $\eta\geq0$ $\quad\psi<0$ $-f_x^4$ $\quad-f_y^4$ $\quad-m_z^4$	$\xi<0$ $\quad\chi\geq0$ $\eta\geq0$ $\quad\psi<0$ $-f_x^1$ $\quad f_y^1$ $\quad m_z^1$	$\xi\geq0$ $\quad\chi<0$ $\eta\geq0$ $\quad\psi<0$ f_x^3 $\quad-f_y^3$ $\quad-m_z^3$	$\xi\geq0$ $\quad\chi\geq0$ $\eta\geq0$ $\quad\psi<0$ f_x^2 $\quad f_y^2$ $\quad m_z^2$
$\xi<0$ $\quad\chi<0$ $\eta<0$ $\quad\psi\geq0$ $-f_x^1$ $\quad-f_y^1$ $\quad-m_z^1$	$\xi<0$ $\quad\chi\geq0$ $\eta<0$ $\quad\psi\geq0$ $-f_x^4$ $\quad f_y^4$ $\quad m_z^4$	$\xi\geq0$ $\quad\chi<0$ $\eta<0$ $\quad\psi\geq0$ f_x^2 $\quad-f_y^2$ $\quad-m_z^2$	$\xi\geq0$ $\quad\chi\geq0$ $\eta<0$ $\quad\psi\geq0$ f_x^3 $\quad f_y^3$ $\quad m_z^3$
$\xi<0$ $\quad\chi<0$ $\eta<0$ $\quad\psi<0$ $-f_x^2$ $\quad-f_y^2$ $\quad-m_z^2$	$\xi<0$ $\quad\chi\geq0$ $\eta<0$ $\quad\psi<0$ $-f_x^3$ $\quad f_y^3$ $\quad m_z^3$	$\xi\geq0$ $\quad\chi<0$ $\eta<0$ $\quad\psi<0$ f_x^3 $\quad-f_y^3$ $\quad-m_z^3$	$\xi\geq0$ $\quad\chi\geq0$ $\eta<0$ $\quad\psi<0$ f_x^4 $\quad f_y^4$ $\quad m_z^4$

Tab. 3: Symmetries of the KBTNH [17], [18]

7 Application cases

Static and dynamic analyses have been performed not only to demonstrate the proper implementation of the non-Hertzian methodology, but also to validate the obtained results and to identify the computational efficiency between the Hertzian and non-Hertzian strategies considered in this work. Here, the bogie of the ML95 vehicle has been used [12], being used the wheel and rail profiles shown in Fig. 9. Note that the wheel profile has been modified to simplify the tread-flange transition, namely, to avoid conformal contact where the contact detection strategy considered in this work cannot be applied. Moreover, the interaction between these profiles results in a nearly Hertzian contact patch which allows the comparison between the results obtained from the non-Hertzian and Hertzian methodologies.
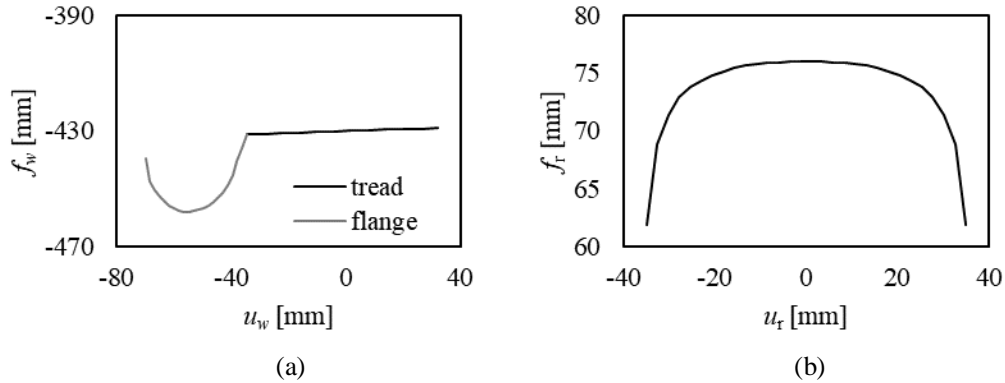

Fig. 9: (a) Wheel and (b) rail profiles

7.1 Static analysis

Three cases have been selected in which the same tread-rail interference occurs, being varied the relative speed in the contact point. The longitudinal and lateral velocities, V_x and V_y, and the pitch and yaw angular velocities, ω_y and ω_z, of the wheelset considered in these cases are listed in Tab. 4. In each case, one of the creepages is magnified. Longitudinal, lateral and spin creepages are promoted for the cases designated as 'Long', 'Lateral' and 'Spin', respectively. Note that residual spin creepage is observed in the 'Long' and 'Lat' cases since the normal vector to the rail, $\mathbf{n}_r^{side}$, and the angular speed vector, $\boldsymbol{\omega}_w$, are not perpendicular. The parameter β is a specified factor to promote the slip, namely, deviations from 1 lead to the increase of the creep forces magnitudes.

14

Case	β	V_x [m/s]	V_y [m/s]	ω_y [rad/s]	ω_z [rad/s]
Longitudinal slip ('Long')	1.0008	10	0	$\beta V_x/R$	0
Lateral slip ('Lat')	1.0010	10	$(1-\beta)V_x$	V_x/R	0
Spin slip ('Spin')	1.4000	10	0	$\beta V_x/R$	$(1-\beta)V_x/H$

Tab. 4: Static cases (R=0.430 [m] and H=0.757 [m])

The contact patch obtained from the three wheel-rail contact models are depicted in Fig. 10(a). Note that the same contact patch is observed for the three case studies as well as the normal contact force as observed in Fig. 10(b) since the slip conditions have no influence on these results. It is observed that the contact patch obtained from the non-Hertzian model is slightly larger than the one obtained by CONTACT as well as the normal contact force. In turn, the contact patch obtained from the Hertzian methodology is bigger than the others since no deformation of the contacting bodies is considered. As consequence, the normal contact force obtained from the Lankarani-Nikravesh (LN) model is the highest, as shown in Fig. 10(b).
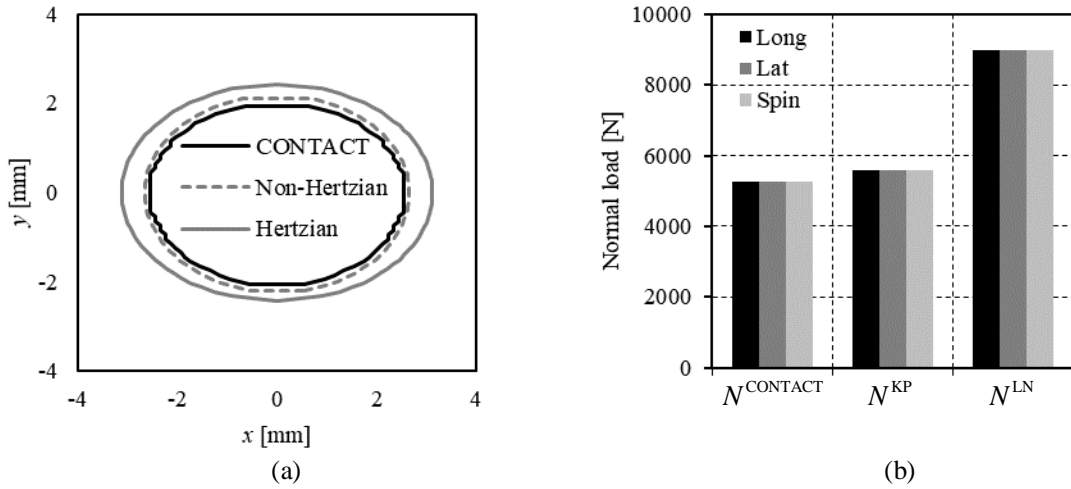

Fig. 10: Comparison of the (a) contact patch and (b) normal contact force

Fig. 11 shows the longitudinal and lateral creep forces for the three case studies. Note that the spin creep moment M_z is not included since the maximum spin creep moment obtained from these cases is residual, namely, lower than 1.3 Nm. In general, a good agreement between the CONTACT and KBTNH model is observed. The Polach method exhibits higher creep forces since higher value of normal contact force obtained from the LN model.

7.2   Dynamic analysis

A multibody model of a bogie that comprises two wheelsets and one bogie frame interconnected by a set of linear spring-damper elements is tested in a tangent track. The bogie starts the simulation with an initial speed of 18 m/s with a misalignment of 2 mm with respect to the centerline, and with a height that avoids initial wheel-rail contact forces. This simulation is run with the Hertzian model presented in [12] and with non-Hertzian methodology proposed in this paper.

Among the results obtained from both methodologies, special attention is put on the lateral motion of the leading wheelset as shown Fig. 12. In general, a good agreement between the two curves is observed. The reduction of the lateral motion is mainly related with the creep forces, but also with the dissipation that occurs in the normal contact force, which is only valid for the 'Hertzian' case since a viscoelastic model is considered. Thus, it is justified the higher reduction of the lateral motion for the 'Hertzian' case. In turn, a close look is put on the first instants of the simulation, as shown in the zoom depicted in Fig. 12. The lateral motion of the wheelset is kept

15

constant and equal 2 mm representing the period that the wheels do not contact the rail. Then, when the wheel-rail contact occurs it is observed that the 'Hertzian' curve adopts the oscillatory motion slightly sooner than the 'Non-Hertzian' curve since it requires less penetration for the stabilization of the forces developed in the contacting surfaces.
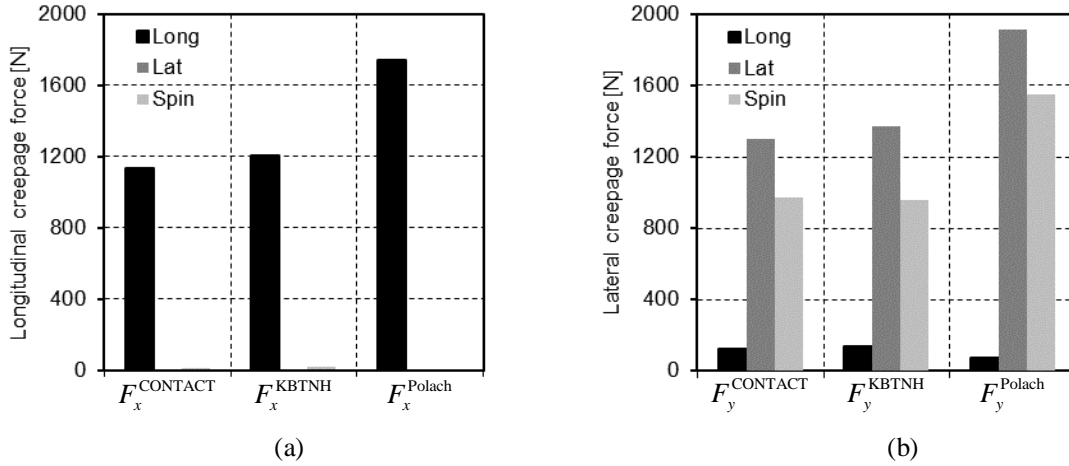

Fig. 11: (a) Longitudinal and (b) lateral creepage forces

From a computational point of view, it has been determined that the 'non-Hertzian' method is approximately 4.5 times slower than the 'Hertzian' method for the presented scenario. Note that the major difference between both methods is that the 'Non-Hertzian' methodology requires an additional time-consuming step due to the contact patch discretization which is the determination of the undeformed distance function.
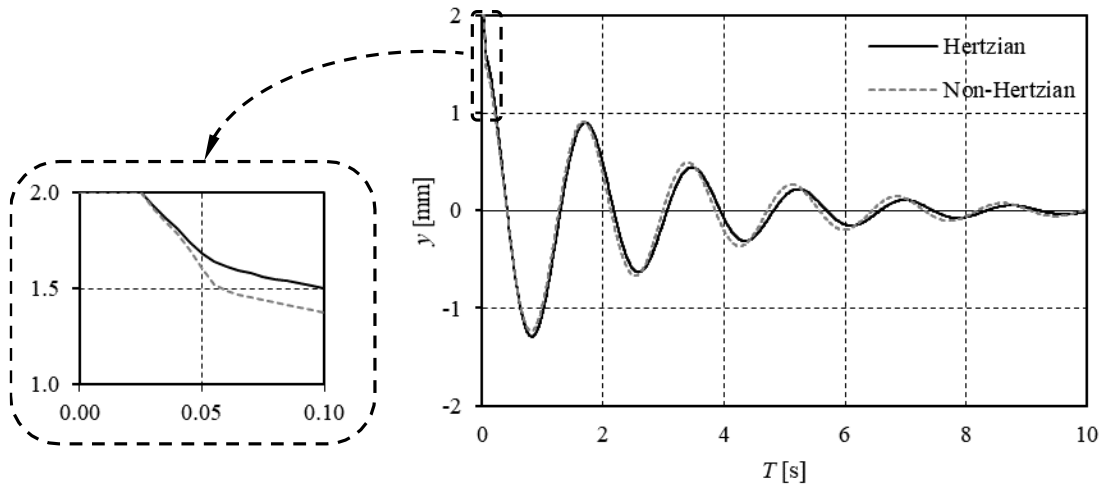

Fig. 12: Lateral motion of the front wheelset

8   Conclusions

The implementation of a non-Hertzian and non-conformal wheel-rail contact model has been presented. The methodology presented here is similar to the one proposed by Pombo *et al* [12], however, the contact patch is determined differently, namely, in this method, the undeformed distance function is calculated. Thus, the presented strategy is more time-consuming, however, it is capable to deal with non-Hertzian contact. To demonstrate the proper implementation of the non-Hertzian strategy, static cases have been performed and compared to the results

obtained from CONTACT in which a good agreement is observed. Then, a dynamic analysis of a bogie negotiating a tangent track has been performed, being discussed these slight differences observed in the results. The proposed methodology showed to be approximately 4.5 times slower, however, it is capable to deal with non-Hertzian contact. As future work, the extension of this method is intended to improve the accuracy of the determination of the contact patch, namely, to take into account the yaw effect [19], and to consider the proper modelling of the conformal contact that has been ignored in this work [20].

Acknowledgements

References

[1]   EN14363, "Railway applications - Testing for the acceptance of running characteristics of railway vehicles - Testing of running behaviour and stationary tests." p. CENELEC European Committee for Electrotechnical St, 2005.

[2]   O. Polach and J. Evans, "Simulations of Running Dynamics for Vehicle Acceptance: Application and Validation," *Int. J. Railw. Technol.*, vol. 2, no. No. 4, p. 59–84 (DOI:10.4203/ijrt.2.4.4), 2013.

[3]   S. Z. Meymand, A. Keylin, and M. Ahmadian, "A survey of wheel–rail contact models for rail vehicles," *Veh. Syst. Dyn.*, vol. 54, no. 3, pp. 386–428, Mar. 2016.

[4]   S. Bruni, J. Vinolas, M. Berg, O. Polach, and S. Stichel, "Modelling of suspension components in a rail vehicle dynamics context," *Veh. Syst. Dyn.*, vol. 49, no. 7, p. 1021–1072 (doi: 10.1080/00423114.2011.586430), 2011.

[5]   H. Magalhães, J. Ambrósio, and J. Pombo, "Railway vehicle modelling for the vehicle–track interaction compatibility analysis," *Proc. Inst. Mech. Eng. Part K J. Multi-body Dyn.*, vol. 230, no. 3, p. 251–267 (doi: 10.1177/1464419315608275), Sep. 2016.

[6]   J. Pombo and J. Ambrósio, "An Alternative Method to Include Track Irregularities in Railway Vehicle Dynamic Analyses," *Nonlinear Dyn.*, vol. 68, no. 1–2, p. 161–176 (doi: 10.1007/s11071–011–0212–2), 2012.

[7]   J. Ambrósio, P. Antunes, and J. Pombo, "On the requirements of interpolating polynomials for path motion constraints," *Mech. Mach. Sci.*, vol. 26, pp. 179–197, 2015.

[8]   P. Antunes, H. Magalhaes, J. Ambrosio, J. Pombo, and J. Costa, "A co-simulation approach to the rail-wheel contact with flexible railways," in *EUROMECH COLLOQUIUM 578 Rolling Contact Mechanics for Multibody System Dynamics*, 2017.

[9]   P. E. Nikravesh, *Computer-Aided Analysis of Mechanical Systems*. Englewood Cliffs, New Jersey: Prentice-Hall, 1988.

[10]   J. J. Kalker, *Three-Dimensional Elastic Bodies in Rolling Contact*. Dordrecht, The Netherlands: Kluwer Academic Publishers, 1990.

[11]   H. Sugiyama and Y. Suda, "On the Contact Search Algorithms for Wheel/Rail Contact Problems," *J. Comput. Nonlinear Dyn.*, vol. 4, no. 4, p. 41001, 2009.

[12]   J. Pombo, J. Ambrósio, and M. Silva, "A New Wheel-Rail Contact Model for Railway Dynamics," *Veh. Syst. Dyn.*, vol. 45, no. 2, p. 165–189 (doi: 10.1080/00423110600996017), 2007.

[13]   M. S. Sichani, R. Enblom, and M. Berg, "Comparison of non-elliptic contact models: Towards fast and

accurate modelling of wheel–rail contact," *Wear*, vol. 314, no. 1–2, pp. 111–117, 2014.

[14]   H. M. Lankarani and P. E. Nikravesh, "A Contact Force Model with Hysteresis Damping for Impact Analysis of Multibody Systems," *AMSE J. Mech. Des.*, vol. 112, pp. 369–376, 1990.

[15]   J. Piotrowski and W. Kik, "A simplified model of wheel/rail contact mechanics for non-Hertzian problems and its application in rail vehicle dynamic simulations," *Veh. Syst. Dyn.*, vol. 46, no. 1–2, pp. 27–48, 2008.

[16]   O. Polach, "A Fast Wheel-Rail Forces Calculation Computer Code," *Veh. Syst. Dyn.*, vol. 33, no. Supplement 33, pp. 728–739, 1999.

[17]   J. Piotrowski, B. Liu, and S. Bruni, "The Kalker book of tables for non-Hertzian contact of wheel and rail," *Veh. Syst. Dyn.*, vol. 55, no. 6, pp. 875–901, Jun. 2017.

[18]   S. Bruni, J. Piotrowski, B. Liu, and E. Di Gialleonardo, "A Fast Method for Determination of Creep Forces in Non-Hertzian Contact of Wheel and Rail Based," 2017.

[19]   B. Liu, S. Bruni, and E. Vollebregt, "A non-Hertzian method for solving wheel–rail normal contact problem taking into account the effect of yaw," *Veh. Syst. Dyn.*, vol. 54, no. 9, pp. 1226–1246, Sep. 2016.

[20]   J. Blanco-Lorenzo, J. Santamaria, E. G. Vadillo, and N. Correa, "On the influence of conformity on wheel–rail rolling contact mechanics," *Tribol. Int.*, vol. 103, pp. 647–667, 2016.